Partial Hydrogenation of 2-Methyl-3-butyn-2-ol over Pd/ZnO

Partial Hydrogenation of 2-Methyl-3-butyn-2-ol over Pd/ZnO: Effect of Reduction Temperature on Alloy Formation and Catalytic Response

Alberto González-Fernández,[a] Chiara Pischetola,[a]

Lioubov Kiwi-Minsker[b,c] and Fernando Cárdenas-Lizana[a,*]

[a]Chemical Engineering, School of Engineering and Physical Sciences, Heriot-Watt University, Edinburgh EH14 4AS, Scotland

[b]Ecole Polytechnique Fédérale de Lausanne (GGRC-ISIC-EPFL), Lausanne CH-1015, Switzerland

[c]Tver State University, Zhelyabova Str., 33, 170100, Tver, Russian Federation

*corresponding author:

e-mail: F.CardenasLizana@hw.ac.uk, tel.: +44(0)131 4514115

Abstract

We have investigated the catalytic effect of β-phase PdZn alloy on selective gas phase hydrogenation of 2-methyl-3-butyn-2-ol (MBY) over Pd/ZnO using Pd/Al_2O_3 as a benchmark. Activation (in H_2) of Pd/ZnO to 973 K generated a β-phase PdZn alloy (from XRD). Five intermediate samples with a modified surface $PdZn/Pd^{\delta-}$ mol ratio (based on XPS) but similar metal nanoparticle size (mean size = 6 nm from HRSEM/STEM) were generated by changing the final activation temperature between 403 K and 973 K. Activation over the same temperature range increased metal nanoparticle size (6 → 10 nm) and lowered the surface $Pd^{\delta-}$ content in the Pd/Al_2O_3 samples. In each case, regardless of the activation temperature, greater selectivity to target 2-methyl-3-buten-2-ol (MBE) was observed over Pd/ZnO relative to Pd/Al_2O_3. Both catalysts delivered a similar activity/selectivity trend characterised by enhanced MBE selectivity and lower activity over the systems activated at higher temperature. We associate this response to formation of β-PdZn alloy and metal encapsulation that impacts on surface $Pd^{\delta-}$ in Pd/ZnO. Pd/ZnO outperformed an industrial Lindlar catalyst, Pd/CuO and Au/Al_2O_3 in terms of selective transformation to MBE. Our results establish the beneficial effect of PdZn alloy phase to promote the continuous production of commercially important alkenols.

1. Introduction

2-Methyl-3-buten-2-ol (MBE) is an important intermediate in the manufacture of vitamins A and E (30,000 tons world production[1] with an expected increasing demand[2]). Industrial synthesis of MBE involves selective hydrogenation of 2-methyl-3-butyn-2-ol (MBY) in pressurised (2-10 bar) batch liquid systems.[3] A transition from batch to continuous operation (at atmospheric pressure) offers clear advantages in terms of energy efficiency and increased productivity for high throughput.[4] The development of continuous systems for MBY hydrogenation is now gaining increasing attention, as shown in the review by Moreno-Marrodan *et al.*.[5] The reaction network for MBY hydrogenation is presented in (**Figure 1**). The main challenge in MBE production is to avoid *over*-hydrogenation (to 2-methylbutanol (MBA)) and oligomerisation.[6]

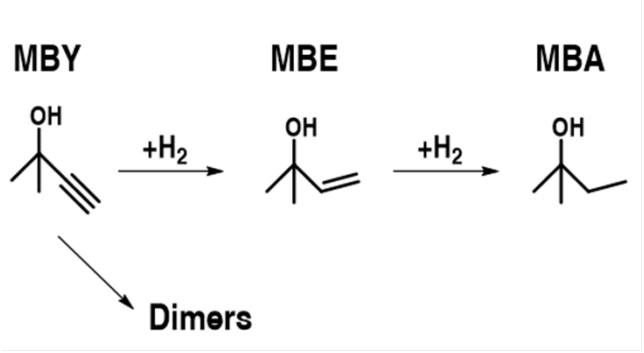

Figure 1: Simplified reaction scheme for the selective hydrogenation of 2-methyl-3-butyn-2-ol (MBY) to target 2-methyl-3-buten-2-ol (MBE) with 2-methylbutanol (MBA) and dimers as undesired reaction by-products from further hydrogenation/oligomerisation.

MBE selectivity is controlled by the relative alkenol/alkynol adsorption strength (A_{ke}/A_{ky}) on metal active sites[7] and favoured at low A_{ke}/A_{ky}[8] (*i.e.*, the alkynol reactant chemisorbs strongly on the catalyst surface and facilitates the desorption of the target MBE by displacement). Palladium has been identified as the best catalytic metal for partial hydrogenation of -C≡C- → -C=C- bond,[9] which can be linked to the low A_{ke}/A_{ky} ratio ($\sim 10^{-3}$)[10] relative to other transition metals typically used in hydrogenation (*e.g.*, A_{ke}/A_{ky} on Pt $\sim 10^{-2}$).[8] Olefin formation is structure

sensitive and favoured over 3-5 nm Pd nanoparticles.[6] Full hydrogenation (to MBA) has been attributed to multi-coordination of MBY[6] on (i) surface defects (*e.g.*, corners and edges) of small (<3 nm) palladium nanoclusters with low electron density ($Pd^{\delta+}$)[6] and (ii) large ensembles of Pd atoms on the crystal planes of palladium nanocrystals >5 nm.[11] A number of strategies have been considered to facilitate the formation of $Pd^{\delta-}$ species and/or reduce Pd ensemble size including: use of basic supports (*e.g.*, MgO and Ga_2O_3),[12] incorporation of an external promoter with a lone pair of electrons (*e.g.*, quinoleine),[13] addition of a second (more electropositive) metal (*e.g.*, Ag, Cu, Pb)[10,14] and/or formation of a homogenous alloy.[15]

Recent studies have shown the potential of a PdZn alloy phase in selective hydrogenation of CO_2 to CH_3OH[16] and semi-hydrogenation of unsaturated hydrocarbons (*e.g.*, dienes,[17] alkynes[18] and alkyndiols[12]). The catalytic application of PdZn catalysts in liquid phase hydrogenation of substituted alkynes has been the subject of appreciable research.[19] However, no attempts have been made to establish a direct correlation between PdZn alloy concentration and catalytic performance, and we have failed to unearth any study in the open literature on continuous alkynol hydrogenation using a supported PdZn alloy catalyst. The synthesis of supported PdZn alloy catalysts can involve the simultaneous loading of both metal precursors on a support (*e.g.*, *co*-impregnation[20] or *co*-precipitation[21]) or loading of a Pd precursor on ZnO (*e.g.*, incipient wetness impregnation)[20] followed by high temperature ($T > 473$ K) activation in H_2.[22] These methodologies suffer from poor control of particle size distribution[23] with a detrimental effect on composition/homogeneity of the PdZn alloy phase formed.[24] A strategy to avoid these issues is the synthesis of size-controlled Pd colloids that can be subsequently deposited on a ZnO support.[25] Altering the final reduction temperature impacts on the degree of support reduction which, in turns, modifies the amount of PdZn alloy phase generated.[26]

In this work, we investigate the effects on catalyst response of PdZn alloy phase in comparison with a standard metallic Pd phase (using Pd/Al_2O_3) in the continuous gas phase hydrogenation of MBY. The impact on catalytic performance of PdZn alloy relative to PdCu (using Pd/CuO) and Pd_3Pb alloy phases (in an industrial Lindlar catalyst) has also been considered. Moreover, as Au has delivered high selectivity in partial -C≡C- bond hydrogenation,[27] we have also studied the catalytic response of Au/Al_2O_3.

2. Experimental Section

2.1. Catalyst Preparation and Activation

The oxide supports, ZnO, Al_2O_3 and CuO were purchased from Sigma-Aldrich and used as received. 1% wt. Pd/ZnO, Pd/Al_2O_3 and Pd/CuO were prepared by deposition of *ex-situ* synthesised monodispersed Pd nanoparticles according to a previously published procedure.[28] An aqueous solution of $PdCl_2$ (Fluka, >99%) and $Na_2MoO_4 \cdot H_2O$ (Fluka, >99%) (Pd/Mo mol ratio = 1) was heated at 368 K under continuous stirring (500 rpm) until complete evaporation. The solid residue was dissolved in water and contacted (at ambient temperature) with a continuous flow of H_2 (100 cm^3 min^{-1}) for 30 min resulting in the formation of uniform Pd nanoparticles stabilised by molybdate anions.[29] Palladium deposition was achieved *via* adsorption where the support (ZnO, Al_2O_3 or CuO; *ca.* 2 g) was immersed and stirred in the Pd colloidal solution for *ca.* 2 h, the slurry filtered and dried in air at ambient temperature. 1% wt. Au/Al_2O_3 was prepared by deposition-precipitation using urea as basification agent. An aqueous mixture of urea (100-fold excess) and $HAuCl_4$ (4.4×10^{-5} mol cm^{-3}) was added to the support (*ca.* 2 g). The suspension was continuously stirred (650 rpm) and heated at 2 K min^{-1} to 353 K, the pH progressively increased to reach *ca.* 7 after 3 h as a result of thermally induced urea decomposition.[30] The solid was separated by centrifugation, washed with deionised water (with centrifugation between each

washing) until chlorine free (confirmed by $AgNO_3$ test) and dried in He (45 cm^3 min^{-1}) at 373 K (2 K min^{-1}) for 5 h. A commercial (5% wt.) Pd(Pb)/$CaCO_3$ (Lindlar catalyst; Pd/$CaCO_3$ poisoned (by impregnation) with lead acetate following a patented method)[31] was purchased from Johnson Matthey. Prior to use, the catalysts were sieved into a batch of 75 μm average diameter and thermally treated in 60 cm^3 min^{-1} H_2 at 10 K min^{-1} to 403-973 K, which was maintained for 1 h. Samples for off-line analysis were passivated in 1% v/v O_2/He at ambient temperature.

2.2. Catalyst Characterisation

The Pd and Au loading was measured by atomic absorption spectroscopy (AAS) using a Shimadzu AA-6650 spectrometer with an air-acetylene flame from the diluted extract in aqua regia (25% v/v HNO_3/HCl). Total specific surface area (SSA), temperature programmed reduction (TPR), and room temperature H_2 chemisorption were determined using a commercial CHEM-BET 3000 (Quantachrome) unit equipped with a thermal conductivity detector (TCD) with data acquisition/manipulation using the TPR WinTM software (Version 1.0a). Total SSA was obtained using the standard single point BET method. The samples were loaded into a U-shaped Quartz cell, outgassed at 423 K for 1 h in 60 cm^3 min^{-1} He and cooled down to room temperature. SSA values were recorded with a 50% v/v N_2/He flow (30 cm^3 min^{-1}); pure N_2 (99.9%) served as the internal standard. At least two cycles of N_2 adsorption–desorption in the flow mode were used to determine total surface area. TPR measurements involved a heating process in 17 cm^3 min^{-1} 5% v/v H_2/N_2 at 10 K min^{-1} to $403 \leq T \leq 973$ K, where the effluent gas passed through a liquid N_2 trap. *Post*-TPR, the thermally treated samples were maintained at the final temperature in a constant flow of H_2/N_2 for 1 h. After TPR, the samples were swept with a flow of N_2 for 1.5 h to remove any physisorbed hydrogen and cooled to room temperature to be

subjected to H_2 chemisorption using a pulse (30 μl) titration procedure. Hydrogen pulse introduction was repeated until the signal area was constant, indicating surface saturation. SSA and H_2 uptake values were reproducible to ±5% and the values quoted in this paper are the mean. Powder X-ray diffractograms (XRD) were recorded on a Bruker/Siemens D500 incident X-ray diffractometer using Cu Kα radiation. The samples were scanned at a rate of 0.02º $step^{-1}$ over the range $20º \leq 2\theta \leq 90º$ (scan time = 5 s $step^{-1}$). Diffractograms were identified using the JCPDS-ICDD reference standard for zincite ZnO (070-8070), γ-Al_2O_3 (153-7011), Pd (046-1043) and β-PdZn (072-2936). Metal nanoparticle size and shape was examined by transmission (TEM), scanning transmission (STEM) and high resolution scanning electron microscopy (HRSEM). TEM measurements were performed using a JEOL JEM 2011 HRTEM unit with a UTW energy dispersive X-ray detector (Oxford Instruments) operated at an accelerating voltage of 200 kV using Gatan DigitalMicrograph 3.4 for data treatment. STEM analysis were conducted in a JEOL 2200FS operated at an accelerating voltage of 200 kV, employing Gatan Digital Micrograph 1.82 for data acquisition/manipulation. HRSEM measurements were carried out in a Zeiss Merlin microscope equipped with a secondary electron detector. The acceleration voltage was 2.5 kV and the working distance was kept at 1.5 mm. Atomic number contrast (*i.e.* "Z contrast") images were obtained with a JEOL 2200FS field emission gun-equipped TEM instrument operated in scanning mode at an accelerating voltage of 200 kV with a nominal 0.5 nm probe size, employing Gatan Digital Micrograph 1.82 for data acquisition/manipulation. By using an annular dark field detector with a minimum collection semi-angle of ~100 mrad, the recorded images have intensity approximately proportional to $tZ^{1.7–2}$ (sample thickness t, average atomic number Z), facilitating a clear contrast between the heavy and lighter element components in the catalyst samples. Up to 300 individual metal particles were counted for each catalyst and the surface area

weighted mean size (d) was calculated from:

$$d = \frac{\sum_i n_i d_i^3}{\sum_i n_i d_i^2} \quad \textbf{(1)}$$

where n_i is the number of particles of diameter d_i. X-ray photoelectron spectroscopy (XPS) analyses were conducted on an Axis Ultra instrument (Kratos analytical, Manchester UK) under ultra-high vacuum condition ($<10^{-8}$ Torr) and using a monochromatic Al Kα X-ray source (1486.6 eV). The source power was maintained at 150 W and the emitted photoelectrons were sampled from a square area of 750 × 350 μm^2; the photoelectron take-off angle was 90°. The analyzer pass energy was 80 eV for survey spectra (0 – 1000 eV) and 40 eV for high resolution spectra (over the Pd 3*d* core level). The carbon 1*s* peak was calibrated at 285.0 eV and used as an internal standard to compensate for any charging effects. Spectra curve fitting and quantification were performed with the Casa XPS software (version 2.3.17), using Shirley background and Gaussian Lorentzian curves with fixed Pd $3d_{5/2}$ position (-5.26 eV) and intensity (+1.5-fold) with respect to Pd $3d_{3/2}$ peak[32] and full width at half maximum (FWHM) of 1.4 eV and 2.4 eV to account for the difference in signal intensity.[33]

2.3. Gas Phase Hydrogenation of 2-Methyl-3-butyn-2-ol (MBY)

Hydrogenation of MBY (Sigma-Aldrich, 99%) was carried out at atmospheric pressure and 403 K after *in situ* catalyst activation in a continuous flow fixed bed tubular reactor (15 mm *i.d.*). Reactions were conducted under operating conditions that ensured negligible mass/heat transport limitations. A layer of borosilicate glass beads served as preheating zone, ensuring that the MBY reactant was vaporised and reached reaction temperature before contacting the catalyst. Isothermal conditions (±1 K) were ensured by diluting the catalyst bed with ground glass (75

μm) before insertion into the reactor. Reaction temperature was continuously monitored by a thermocouple inserted in a thermowell within the catalytic bed. Pure MBY was delivered to the reactor at a fixed calibrated flow rate (1.2 cm^3 h^{-1}) *via* a glass/teflon airtight syringe and teflon line using a microprocessor controlled infusion pump (Model 100 kd Scientific). A co-current flow of MBY and H_2 (<1% v/v organic in H_2) was maintained at a $GHSV = 2 \times 10^4$ h^{-1} with a molar metal (Pd or Au) to inlet reactant molar feed rate (n/F) of 4×10^{-7} - 11×10^{-6} h. The H_2 content was in excess of the stoichiometric requirement for full hydrogenation (to MBA), the flow rate was monitored using a Humonics (Model 520) digital flowmeter. In a series of blank tests, passage of MBY in a stream of H_2 through the empty reactor or over each support alone did not result in any detectable conversion. The reactor effluent was condensed in an ice-cold water trap for subsequent analysis, which was made using a Perkin-Elmer Auto System XL gas chromatograph equipped with a programmed split/splitless injector and a flame ionisation detector, employing a Stabilwax (Cross-Bond Carbowax-PEG; 30 m × 0.32 mm *i.d.*, 0.25 μm film thickness) capillary column (Restek). Data acquisition and manipulation were performed using the TurboChrom Workstation Version 6.3.2 (for Windows) chromatography data system. MBY, MBE and MBA (Sigma-Aldrich, ≥98%) were used as supplied without further purification. All the gases (O_2, H_2, N_2 and He) employed were of ultra high purity (BOC, >99.98%). Reactant and product molar fractions (x_i) were obtained using detailed calibration plots (not shown). MBY conversion (X_{MBY}) was obtained from

$$X_{MBY}(\%) = \frac{[MBY]_{in} - [MBY]_{out}}{[MBY]_{in}} \times 100 \quad \textbf{(2)}$$

and selectivity in terms of MBE (S_{MBE}) as target product is given by

$$S_{MBE}(\%) = \frac{[MBE]_{out}}{[MBY]_{in} - [MBY]_{out}} \times 100 \quad \textbf{(3)}$$

where the subscripts "in" and "out" refer to the inlet and outlet gas streams. Catalytic activity is also quantified in terms of MBY transformation rate (R_{MBY}, mol mol_{Pd}^{-1} s^{-1}) obtained from time on-stream measurements, using MBY conversion (*ca.* 5-10%) at steady-state condition:

$$R_{MBY}\ (\text{mol mol}_{Pd}^{-1}\ \text{s}^{-1}\ ) = \frac{X_{MBY} \cdot F}{100 \cdot n} \quad \textbf{(4)}$$

Turnover frequency (*TOF*, rate per active site, s^{-1}) was calculated using metal dispersion (*D*) values from microscopy analysis according to:

$$TOF\ (\text{s}^{-1}\ ) = \frac{R_{MBY}}{D} \quad \textbf{(5)}$$

Repeated reactions with different samples from the same batch of catalyst delivered raw data reproducibility and carbon mass balances that were within ±5%.

3. Results and Discussion

3.1. Pd/ZnO vs. Pd/Al_2O_3

3.1.1. Catalyst Characterisation

Table 1: Physico-chemical properties of Pd/ZnO, Pd/Al_2O_3, Au/Al_2O_3, Pd/CuO and Lindlar catalysts.

		Pd/ZnO	**Pd/Al_2O_3**	**Au/Al_2O_3**	**Pd/CuO**	**Lindlar**
Metal loading (wt. %)		1.0	0.9	1.1	1.1	5.0
SSA (m^2 g^{-1})		8	157	166	20	10
TPR	T_{max} (K)[a]	*335*, 685	*335*	448	*333*,525	*340*
	H_2 consumption (μmol g^{-1})	2103[b]	-	87[b]/84[c]	11300[b]	-
H_2 uptake (μmol g_{metal}^{-1})[d]		167[e]/85[f]	1560[e]/1020[f]	32[e]	75[e]	217[g]
d (nm)		6[h]/6[f]	6[h]/10[f]	4[e]	5[e]	4[g]
D (%)		18[h]/18[f]	18[h]/11[f]	30[e]	22[e]	27[g]

[a]T_{max} associated with negative TPR peak is given in italic; [b]experimental value; [c]theoretical H_2 consumption for $Au^{3+} \rightarrow Au^0$; [d]hydrogen chemisorption at room temperature; [e]catalyst activated in hydrogen at 573 K; [f]catalyst activated in hydrogen at 973 K; [g]catalyst activated in hydrogen at 603 K; [h]fresh catalyst.

Total specific surface area (SSA) of the ZnO (10 m^2 g^{-1}) and Al_2O_3 (173 m^2 g^{-1}) supports are in accord with values in the literature for zincite ZnO (4-10 m^2 g^{-1})[34] and gamma-phase alumina

(140-190 m^2 g^{-1}).[35] The introduction of Pd colloids resulted in lower values of SSA (**Table 1**), suggesting pore blockage by the metal component.[36] The TPR profiles for Pd/ZnO **(A)**, Pd/Al_2O_3 **(B)** and ZnO **(C)** are presented in **Figure 2**. While the TPR response for the ZnO support was featureless (*i.e.* no evidence of H_2 uptake/release), the supported catalysts show a hydrogen released (negative peak) at 335 K that can be linked to room temperature Pd β-hydride decomposition;[37] room temperature palladium precursor reduction to Pd^0 has been established elsewhere.[38] Hydride composition in terms of H/Pd molar ratio depends on Pd nanoparticle size.[39] We observe a similar value for both catalysts (~0.20) consistent with formation of well dispersed nano-scale (4-6 nm) palladium particles.[39] TPR of Pd/ZnO exhibits a broad positive signal over the range 475-775 K. The amount of hydrogen associated with the single consumption peak (T_{max} at *ca.* 685 K) was significantly lower (by a factor of 6) than that required to fully reduce ZnO to metallic zinc and suggests that the presence of Pd results in "partial" ZnO → Zn reduction at the metal-support interface[40] with formation of a PdZn alloy phase.[12]

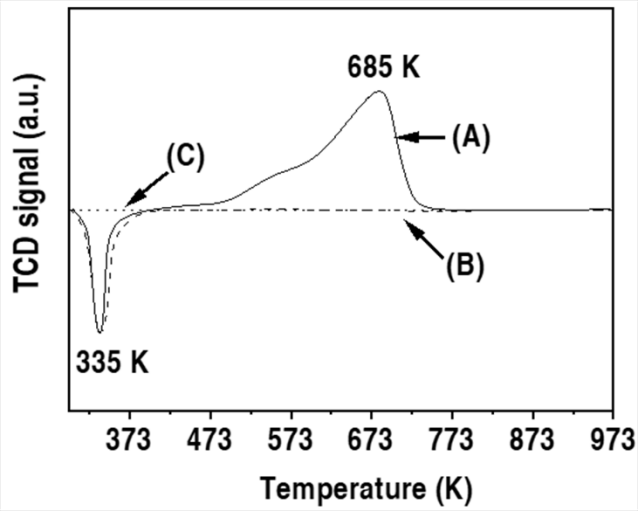

Figure 2: TPR profiles for **(A)** Pd/ZnO (solid line), **(B)** Pd/Al_2O_3 (dashed line) and **(C)** ZnO (dotted line).

XRD analysis was used to examine crystal properties and confirm PdZn alloy formation;

results for the ZnO **(I)** and Al_2O_3 **(II)** systems are presented in **Figure 3**.

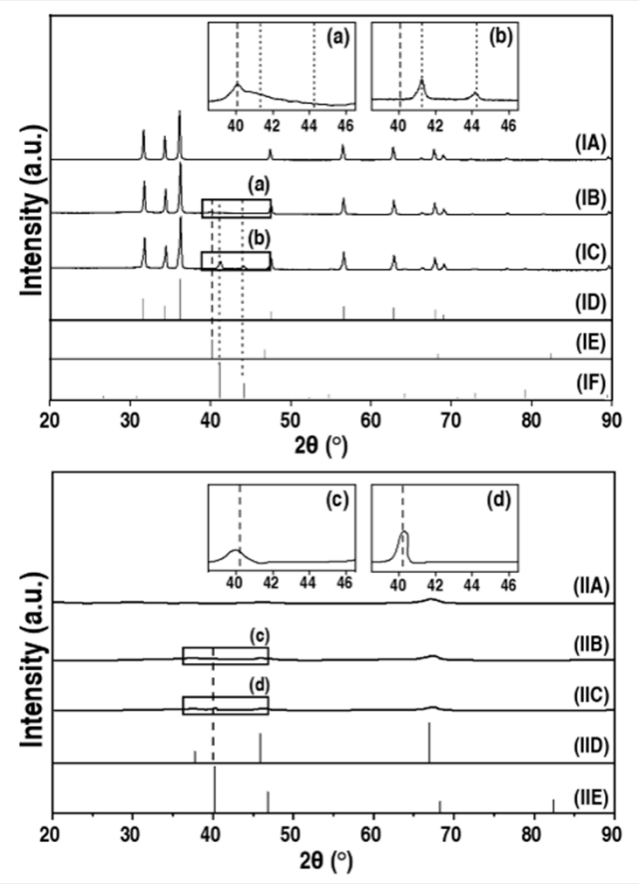

Figure 3: XRD patterns associated with **(I)** ZnO **(A)**, Pd/ZnO fresh **(B)** and after hydrogen thermal treatment to 973 K **(C)**, JCPDS-ICDD reference for **(D)** zincite-ZnO (070-8070), **(E)** Pd (046-1043) and **(F)** β-PdZn (072-2936); **(II)** Al_2O_3 **(A)**, Pd/Al_2O_3 fresh **(B)** and after treatment to 973 K **(C)**, JCPDS-ICDD reference for **(D)** γ-Al_2O_3 (153-7011) and **(E)** Pd (046-1043). *Note*: XRD diffractogram magnifications over *ca.* 2θ = 38-46° for patterns **(IB)**, **(IC), (IIB)** and **(IIC)** is presented as insets **(a)**, **(b), (c)** and **(d)**, respectively. Dashed line identifies position of the Pd^0 main peak (2θ = 40.1°) while dotted lines illustrate the position of characteristic peaks for β-PdZn (2θ = 41.2° and 44.1°).

Selected areas in the diffractogram of Pd/ZnO fresh **(IB)** and *post*-TPR to 973 K **(IC)** have been magnified and are shown as insets **(a)** and **(b)**, respectively. The as-received ZnO support **(IA)** presents sharp signals at 2θ = 32.1°, 34.5°, 36.5°, 47.8°, 57.2°, 63,1°, 68.5° and 69.8° corresponding to the (1 0 0), (0 0 2), (1 0 1), (1 0 2), (2 -1 0), (1 0 3), (2 -1 2) and (2 0 1) planes of hexagonal close-packed (*hcp*) zincite **(ID)**. The XRD pattern for all the Pd/ZnO samples

exhibited the diffraction peaks observed in **(IA)** with an additional reflection at $2\theta = 40.1°$ in **(IB)** (see inset **(a)**) due to the (1 1 1) main plane of metallic Pd **(IE)**. *Post*-TPR at 973 K **(IC)** the XRD reflection of Pd^0 at $2\theta = 40.1°$ disappears while we observe the simultaneous appearance of XRD signals at $2\theta = 41.2°$ and 44.1° (see inset **(b)**) characteristic of hexagonal (β-phase) PdZn alloy **(IF)**. A stable β-PdZn alloy phase can be formed at $T \geq 373$ K during heating treatment in hydrogen.[17,41] The comparable intensity for the main peak in **(a)** and **(b)** observed for Pd/ZnO fresh and activated at 973 K is indicative of similar metal dispersion. This is consistent with reports in the literature that have shown absence of metal agglomeration for (2-7 nm) Cu,[42] Au[43] and Pt[44] nanoparticles supported on ZnO after activation up to $T = 873$ K. Oxygen vacancies are surface defects generated by the loss of lattice oxygen due to high temperature chemical reduction in hydrogen (*ca.* 738 K for ZnO[45] and 550 K on Pd/ZnO[46]). The lack of metal sintering can be linked to strong interaction of Pd with surface defects on ZnO. Moreover, β-PdZn alloy at the metal-support interface[47] can also serve to anchor Pd nanoparticles inhibiting metal mobility. The XRD pattern of the *as*-received alumina support **(IIA)** presents a broad reflection at $2\theta = 66.9°$ associated with the (4 4 0) main plane of cubic γ-Al_2O_3 **(IID)**. The XRD diffractograms of the fresh (**IIB**) and activated (to 973 K) Pd/Al_2O_3 (**IIC**) show an additional peak at $2\theta = 40.1°$ (see inset **(c)** and **(d)**) characteristic of Pd^0 (see profile **(IIE)**). The main Pd^0 peak in Pd/ZnO (**(IB)** and inset **(a)**) and Pd/Al_2O_3 (**(IIB)** and inset **(c)**) has a similar intensity and width. In contrast, the activated Pd/Al_2O_3 exhibits a sharper peak (*i.e.* higher intensity and smaller width) suggesting Pd particle growth. A weaker interaction between (*non*-reducible) Al_2O_3 (*vs.* reducible ZnO) and Pd is consistent with the lower adhesion energy ($E_{ads,\ Pd\text{-}Al_2O_3}$ = 0.3-1.59 J m^{-2} *vs*. $E_{ads,\ Pd\text{-}ZnO}$ = 2.3-2.5 J m^{-2})[48] and can result in metal surface diffusion and particle sintering.

Metal particle morphology was further examined by microscopy analyses, representative TEM, SEM and STEM images of (unsupported) Pd nanoparticles and (supported) fresh and activated to 973 K (as a representative) Pd/ZnO and Pd/Al_2O_3 are presented in **Figure 4**; associated metal particle size histograms are shown in **Figure 5**.

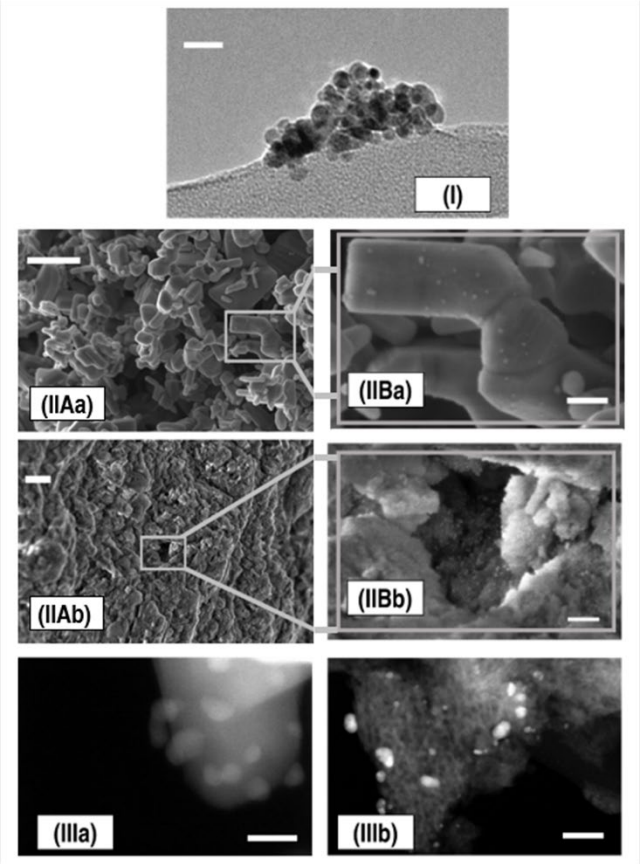

Figure 4: Representative **(I)** TEM image of Pd colloids (scale bar = 20 nm); **(II)** SEM micrographs at medium **(A)** (scale bar = 100 nm) and high-resolution **(B)** (scale bar = 20 nm) for fresh **(a)** Pd/ZnO and **(b)** Pd/Al_2O_3; **(III)** STEM image of **(a)** Pd/ZnO (scale bar = 20 nm) and **(b)** Pd/Al_2O_3 (scale bar = 50 nm) after H_2 treatment to 973 K.

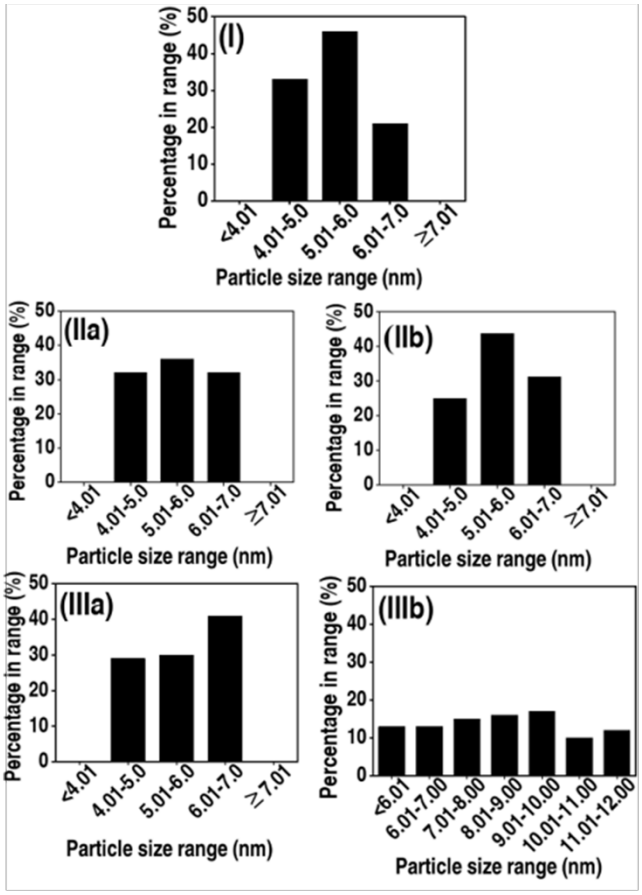

Figure 5: Metal particle size histograms associated with **(I)** Pd colloids, **(II)** fresh and **(III)** *post*-thermal treatment in H_2 to 973 K **(a)** Pd/ZnO and **(b)** Pd/Al_2O_3.

SEM analysis of Pd/ZnO (**Figure 4(IIa)**) shows an aggregation of small crystallites (≤40 nm) with a rod-like structure characteristic of zincite-ZnO.[49] The alumina carrier presents a more amorphous structure (**Figure 4(IIb)**), a result that is in line with the broad diffraction peak observed by XRD analysis (**Figure 3(II)**). The representative TEM image of Pd colloids (**Figure 4(I)**) demonstrates the formation of quasi-spherical nanoparticles with a narrow (4-7 nm; **Figure 5(I)**) size distribution and mean size (=5 nm). This is consistent with morphology (shape and size) reported elsewhere[28] for Pd colloids synthesised by a similar method. The SEM micrographs (**Figure 4(II)**), size distribution histograms (**Figure 5(II)**) and entries in **Table 1** demonstrate that deposition of Pd on the ZnO and Al_2O_3 supports had little effect on palladium

nanoparticle shape or size for the fresh samples. The integrity of the metal nanocrystals was maintained in Pd/ZnO with no significant changes in size/shape *post*-activation to 973 K (**Figure 4(IIIa)**, **Figure 5(IIIa)** and **Table 1**). In contrast, we observed an increase in nanoparticle size for Pd/Al_2O_3 after thermal treatment to high temperature (from 6 → 10 nm; **Figure 4(IIIb)**, **Figure 5(IIIb)** and **Table 1**) that is consistent with XRD measurements and reported literature showing metal sintering at $T > 575$ K for Al_2O_3 supported metal catalysts[50] and Pd colloids supported on *non*-reducible carriers.[51] XRD provides information on bulk characteristics which can differ significantly from surface properties.[52] XPS analysis can provide critical information on surface Pd content/charge and PdZn alloy formation.[53] The fitted Pd 3*d* envelope for **(I)** Pd/ZnO and **(II)** Pd/Al_2O_3, activated in H_2 to 973 K, as representative examples, are shown in **Figure 6**. Both catalysts present an XPS spectrum characterised by a doublet with Pd $3d_{5/2}$ binding energy (BE) = 334.6 ± 0.1 eV and Pd $3d_{3/2}$ BE = 339.9 ± 0.1 eV that are *ca.* 0.5 eV lower than those characteristic of Pd^0 (Pd $3d_{5/2}$ BE = 335.1 eV and Pd $3d_{3/2}$ BE = 340.4 eV [54]). This suggests electron transfer from the carrier to Pd resulting in a partial negatively charged metal phase ($Pd^{\delta-}$). A similar downshift in BE have been previously reported for (2-10 nm) Pd nanoparticles[56] and ascribed to electron transfer from the oxide carrier.[55] The spectrum of each catalyst exhibits a doublet at higher BE (Pd $3d_{5/2}$ = 337.0 ± 0.5 eV and Pd $3d_{3/2}$ = 342.2 ± 0.5 eV) characteristic of surface Pd^{2+} species that can result from surface oxidation during the passivation step.[52] The XPS spectrum of Pd/ZnO presents an additional doublet at values of BE equal to 335.7 eV (Pd $3d_{5/2}$) and 340.9 eV (Pd $3d_{3/2}$) that is characteristic of PdZn alloy.[53]

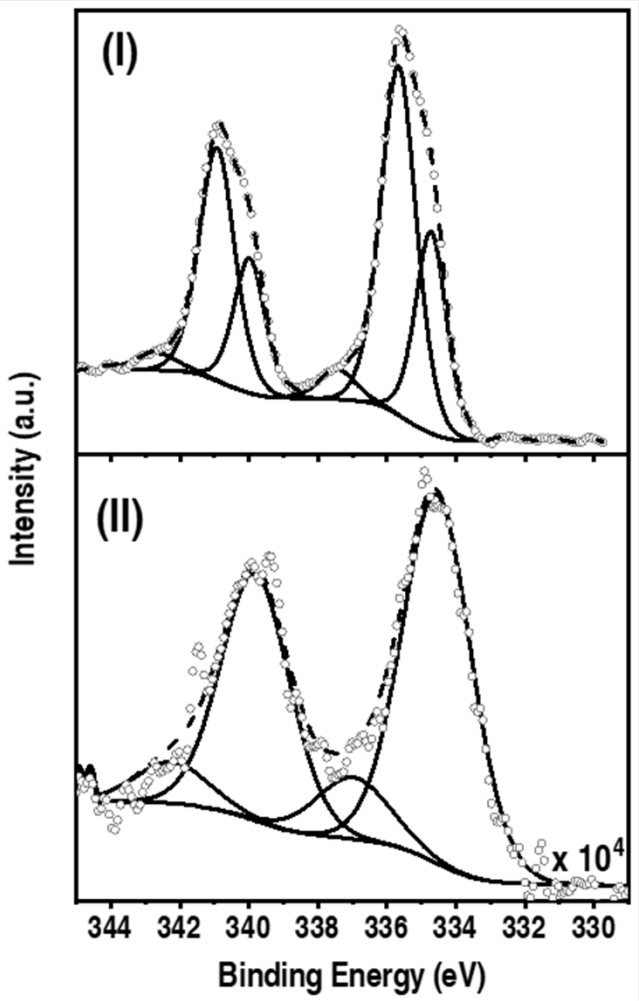

Figure 6: XPS profile over the Pd 3*d* region for thermally treated (to 973 K) in hydrogen (**I**) Pd/ZnO and (**II**) Pd/Al_2O_3. *Note*: Raw data are shown as open symbols (○) while curve fitted and envelope are represented by solid and dashed lines, respectively.

The XRD results suggest that increased activation temperature facilitates PdZn alloy formation. In order to explicitly demonstrate change(s) in the surface composition of the active sites due to thermal treatment, we have plotted the surface content of $Pd^{\delta-}$ and PdZn species (balance close with Pd^{2+} content; 5 ± 2%) obtained from XPS analysis, as a function of activation temperature and the results are presented in **Figure 7.**

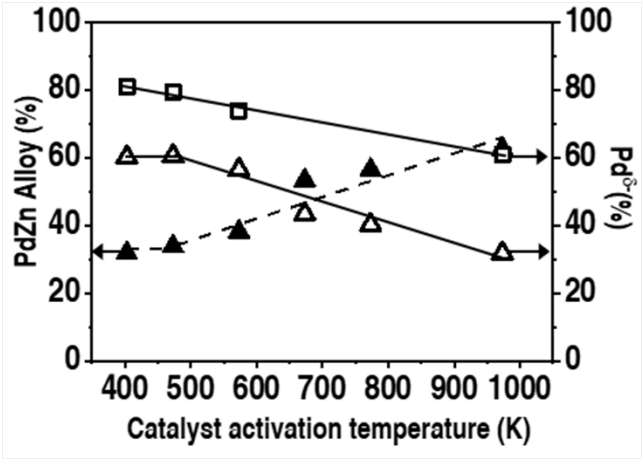

Figure 7: Variation in surface $Pd^{\delta-}$ (open symbols) and PdZn alloy content (solid symbols) with activation temperature for Pd/ZnO (△, ▲) and Pd/Al_2O_3 (□). *Note:* solid and dashed lines provide a guide to aid visual assessment.

We recorded a PdZn content of *ca*. 30% for Pd/ZnO activated at 403-473 K. A similar temperature requirement (≥373 K) has been shown by XANES and EXAFS for PdZn alloy phase formation.[17] A greater PdZn alloy content (30 → 63%) was accompanied by a decrease in the amount of $Pd^{\delta-}$ (from 60% to 32%) with increasing activation temperature. Pd/Al_2O_3 exhibited a (*ca.* 25%) decrease in the surface concentration of $Pd^{\delta-}$ with activation temperature (403 K → 973 K) (**Figure 7**) that can be ascribed to particle sintering. Gigola *et al.*,[57] observed the same temperature dependence and reached a similar conclusion for CeO_2-Pd/α-Al_2O_3. In each case, the concentration of $Pd^{\delta-}$ for Pd/Al_2O_3 was greater than that recorded for Pd/ZnO (60-80% *vs.* 32-60%) activated at the same temperature.

Hydrogen chemisorption analysis is of practical importance in hydrogenation applications. We recorded a total hydrogen uptake in the range 85-1560 μmol g_{Pd}^{-1} on Pd/ZnO and Pd/Al_2O_3 activated up to 973 K (**Table 1**) in line with reported values (234-2380 μmol g_{Pd}^{-1}) for Pd/ZnO[58] and Pd/Al_2O_3[59] with similar metal content. We observed a decrease in uptake with increasing activation temperature, with lower values for Pd/ZnO *vs.* Pd/Al_2O_3. This is consistent

with published work where β-PdZn alloy phase has exhibited limited hydrogen chemisorption capacity[58] and particles bearing a greater $Pd^{\delta-}$ content have shown to enhance H_2 adsorption/activation.[60] While the nature of the palladium phase can impact directly on hydrogen chemisorption, there is also the possibility of an indirect contribution *via* "metal encapsulation". The latter is possible through the formation of a ZnO_{1-x} layer *post*-H_2 treatment to $T \geq 373$ K[46] that covers partially the palladium sites and inhibits hydrogen uptake.

3.1.2 Catalytic Response

The effect of catalyst activation temperature on MBY hydrogenation activity **(I)** and MBE selectivity **(II)** response over Pd/ZnO and Pd/Al_2O_3 is presented in **Figure 8**. Both catalysts undergo an induction period where activity declines to attain a steady state conversion after *ca.* 90 minutes on-stream (see inset in **Figure 8(I)**) showing a similar activity dependence characterised by a decrease in hydrogenation rate with activation temperature where greater values were observed for Pd/Al_2O_3 (*vs.* Pd/ZnO) at each activation temperature. -C≡C- bond hydrogenation over supported Pd has been proposed to follow the Horiuti-Polanyi mechanism consistent with a sequential alkyne → alkene → alkane conversion.[61] Atomic hydrogen, formed through dissociative H_2 chemisorption on palladium, acts as weak electrophilic agent and attacks (in two sequential steps) the triple bond.[62] The addition of the second H is rate limiting[63] and sensitive to hydrogen coverage on the metal surface[64] (*i.e.* higher concentration of surface hydrogen lowers the activation energy barrier).[11] The greater activity over samples activated at lower temperature and Pd/Al_2O_3 (*vs*. Pd/ZnO) can be tentatively linked to an enhanced hydrogen chemisorption capacity (**Table 1**) due to higher surface $Pd^{\delta-}$ content (**Figure 7**). Catalytic activity was insensitive to activation temperature at $T \leq 473$ K, the temperature range over which we observed an almost constant $Pd^{\delta-}$ concentration

in Pd/ZnO (~60%) and Pd/Al_2O_3 (~80%) (**Figure 7**). Activation at $T > 473$ K resulted in a concomitant decrease in activity (R_{MBY}), $Pd^{\delta-}$ and H_2 chemisorption. This can be ascribed to β-PdZn alloy formation and (partial) metal encapsulation for Pd/ZnO and metal sintering for Pd/Al_2O_3, as demonstrated by XPS, XRD and microscopy analyses.

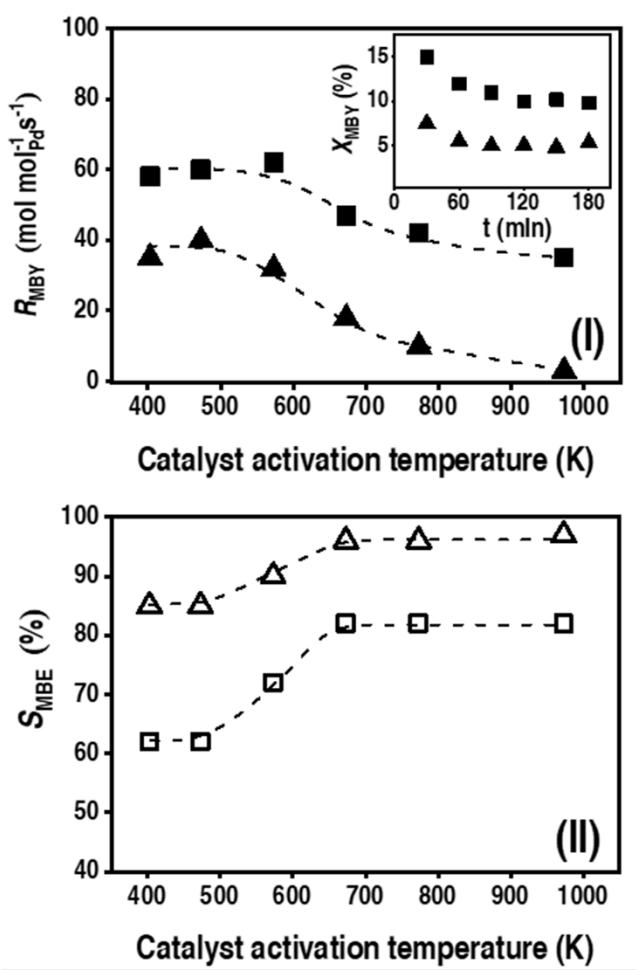

Figure 8: Variation of **(I)** MBY transformation rate (R_{MBY}, mol mol_{Pd}^{-1} s^{-1}; solid symbols) and **(II)** MBE selectivity (S_{MBE}, %; open symbols) with catalyst activation temperature over Pd/ZnO (▲,△) and Pd/Al_2O_3 (■, □). *Inset in* **(I)***:* Variation of MBY conversion (X_{MBY}) with time on-stream for reaction over Pd/ZnO (▲) and Pd/Al_2O_3 (■) activated at 573 K, as representative samples. *Reaction conditions*: $T = 403$ K, $P = 1$ atm, $X_{MBY} \sim 10\%$.

We conducted a series of experiments to examine the effect(s) of β-PdZn alloy formation on reaction selectivity at the same degree of conversion and the results are given in **Figure 8(II)**. The conversion of MBY over Pd/ZnO and Pd/Al_2O_3 generated MBE and MBA as the only

products. There were no detectable oligomerisation products (**Figure 1**), a result that deviates from -C≡C- bond gas-phase hydrogenation of alkynes (*e.g.*, acetylene)[10] over (SiO_2 and zeolite) supported Pd catalysts.[65,66] The absence of oligomer formation in this work can be the result of high H_2:Alkyne ratio[10] (*i.e.*, alkyne condensation is hampered at low surface alkyne concentrations)[67] and presence of Lewis basic sites on Al_2O_3 and ZnO[68,69] (*i.e.*, oligomerisation is promoted in the presence of metal cations of strong acid supports).[70] We observed higher selectivity (*ca.* 25%) to the target MBE over Pd/ZnO (*vs.* Pd/Al_2O_3) at each activation temperature. Both (Al_2O_3 and ZnO supported) systems exhibit a similar S_{MBE} *vs.* activation temperature dependence characterised by three main regions: (i) low S_{MBE} (≤85%) for catalysts activated at $T \leq 473$, (ii) enhanced S_{MBE} (70-90 %) for samples reduced over $473 \leq T < 673$ K and (iii) highest S_{MBE} (up to 97%) for systems thermally treated in hydrogen at $T > 673$ K. The high selectivity achieved in this work is an important result on the light of the lower S_{MBE} values reported for MBY hydrogenation over Pd/ZnO in pressurised (3-10 bar) batch systems.[71] Pd/ZnO and Pd/Al_2O_3 bear metal particles of similar size (*ca*. 6 nm) upon activation at low temperatures (≤473 K) although the formation of β-PdZn alloy (**Figure 7**) can reduce the size of $Pd^{\delta-}$ ensembles on metal crystal planes (responsible for MBY multi-complexation and undesired MBA formation)[15] resulting in greater olefin selectivity. An increase in PdZn alloy concentration following activation between 473 and 673 K (**Figure 7**) further reduces palladium ensemble size increasing S_{MBE}. Over the same range of activation temperatures Pd/Al_2O_3 undergoes metal sintering (6 → 10 nm) which lowers the concentration of surface defects,[72] responsible for over-hydrogenation.[6] The almost constant MBE selectivity for samples activated at $T > 673$ K is consistent with minor variations in PdZn alloy content (60 ± 3%, **Figure 7**) on Pd/ZnO and percentage of surface defects for metal particles with $d > 8$nm[73] for Pd/Al_2O_3.

3.2. Pd/ZnO vs. Pd/CuO vs. Au/Al_2O_3 vs. Lindlard Catalyst

3.2.1. Catalyst Characterisation

The SSA of Au/Al_2O_3, Lindlar and Pd/CuO are recorded in **Table 1**. The TPR activation profiles of the three catalysts are given in **Figure 9** while the temperatures associated with maximum H_2 desorption/consumption are provided in **Table 1**.

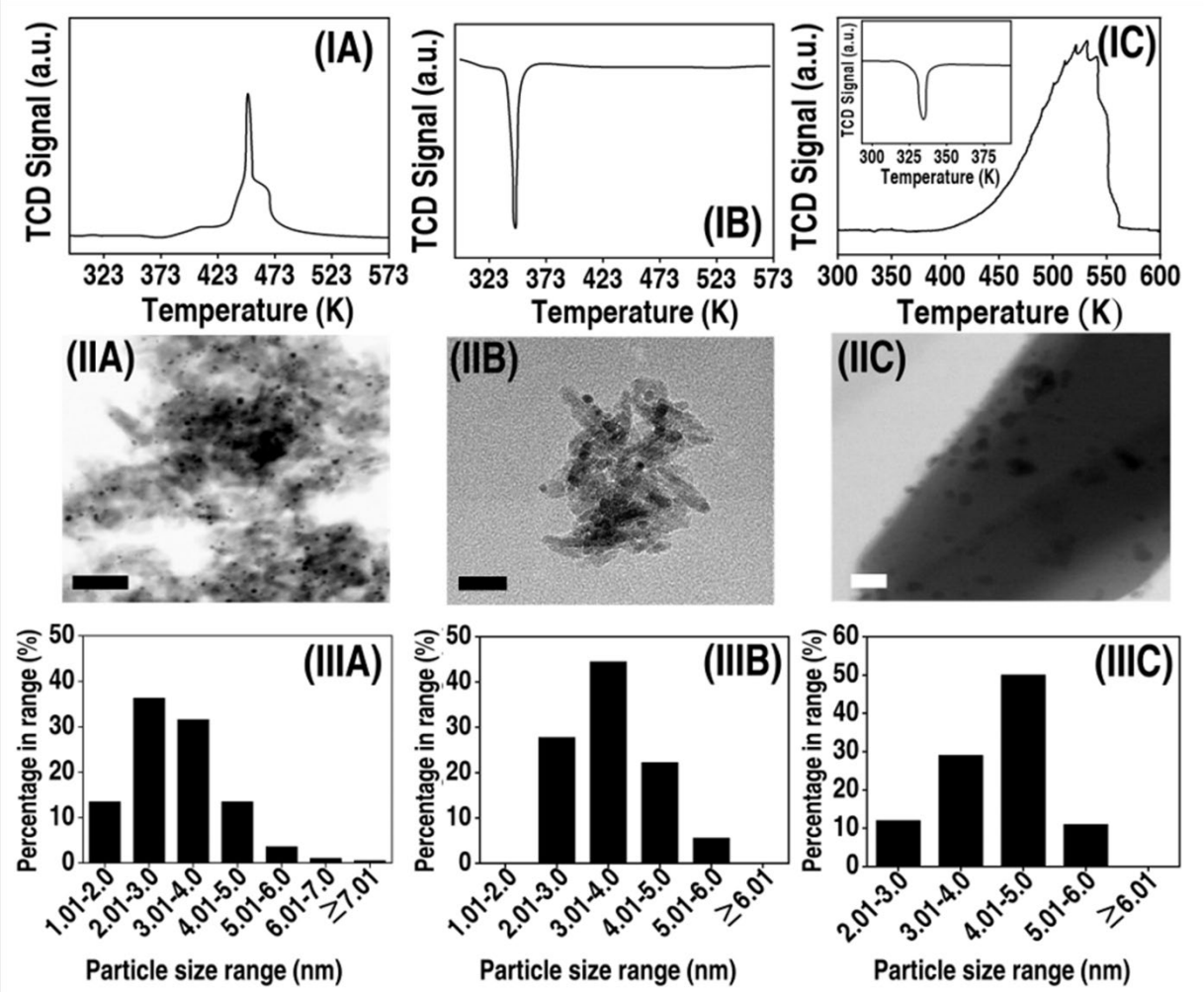

Figure 9: **(I)** TPR profiles and **(II)** representative TEM/STEM images (scale bar = 20 nm) with **(III)** associated metal particle size histogram for **(A)** Au/Al_2O_3, **(B)** Lindlar's and **(C)** Pd/CuO catalysts. *Note:* TPR profile magnification over *ca.* 295 K ≤ *T* ≤ 395 K for **(IC)** is included as an inset.

Au/Al_2O_3 **(IA)** shows a single positive peak at T_{max} = 448 K with experimental hydrogen

consumption matching that required for complete Au^{3+} to Au^0 reduction.[74] Hao *et al.*[75] demonstrated (by XPS analysis) the formation of metallic gold in Au/Fe_2O_3 after thermal treatment (in H_2) to 573 K. The negative peak at 333-340 K in the TPR profiles of Lindlar **(IB)** and Pd/CuO **(IC)** catalysts can also be linked to Pd β-hydride decomposition. The equivalent H/Pd molar ratio for the Lindlar catalyst (0.17 *vs.* 0.20) suggests a similar Pd nanoparticle size to that recorded for Pd/ZnO and Pd/Al_2O_3 (*i.e.*, 6 nm). Pd/CuO exhibited a lower H/Pd ratio (~0.05), a result that can be linked to Pd encapsulation due to the room temperature formation of $PdCuO_{1-x}$ species[76] that reduce H_2 diffusion into Pd bulk phase[77] lowering H/Pd. We observed a significantly lower surface Pd content (from XPS elemental analysis) relative to AAS loading (0.2 *vs.* 1 wt.%) for Pd/CuO which further suggests metal encapsulation by CuO. TPR of Pd/CuO shows a positive peak at *ca.* 425-560 K with a T_{max} = 525 K characteristic of $CuO \rightarrow Cu^0$.[78] The lower band gap of CuO (1.2 eV)[79] relative to ZnO (3.3 eV)[80] results in greater reducibility[76] and can account for the downshift in the temperature requirement (by 160 K; see **Figures 2(A)** *vs.* **Figure 9(IC)**) for CuO reduction. The hydrogen uptake for Au/Al_2O_3 (32 μmol g_{Au}^{-1}) was low, in line with the high activation energy barrier of H_2 dissociative adsorption due to the filled *d* band.[81] Hydrogen chemisorption on Pd Lindlar (217 μmol g_{Pd}^{-1}) and Pd/CuO (75 μmol g_{Pd}^{-1}) was significantly lower (up to a 20-fold) than that recorded for Pd/Al_2O_3 activated at a similar temperature (**Table 1**), which can be linked to Pd coverage by $Pb(OAc)_2$ during catalyst synthesis[31] and PdCu alloy formation *post*-TPR at $T \geq 438$ K.[82]

A representative high-resolution STEM image of Au/Al_2O_3 is given in **Figure 9(IIA)** with associated nanoparticle size histogram in **Figure 9(IIIA)**. The catalyst exhibits pseudo-spherical Au nanoparticles in the 1–8 nm size range with a mean diameter of 4 nm (**Table 1**). Low-coordination surface sites (*e.g.*, corner, steps and edges) in gold nanoparticles ≤5 nm have been

identified as active sites for hydrogen adsorption/activation[83] and are essential for significant activity in hydrogenations.[84] The representative STEM images of Pd Lindlar **(IIB)** and Pd/CuO **(IIC)** are shown in **Figure 9**. Metal particles of globular morphology in the 2- 6 nm size range are in evidence (**Figure 9(IIIB-IIIC)**), with a mean Pd particle size of 4 nm (Lindlar) and 5 nm (Pd/CuO) (**Table 1**).

3.2.2. Catalytic Response

In this study, catalytic performance of Pd/ZnO was compared with other well-known selective catalysts for alkyne hydrogenation including Au/Al_2O_3 and Pd alloys (Pd_3Pb in Lindlar catalyst and PdCu in Pd/CuO). We first examined the catalytic performance of Pd/ZnO *vs.* Pd/CuO *vs.* Au/Al_2O_3 under the same reaction conditions and the results obtained are presented in **Figure 10**.

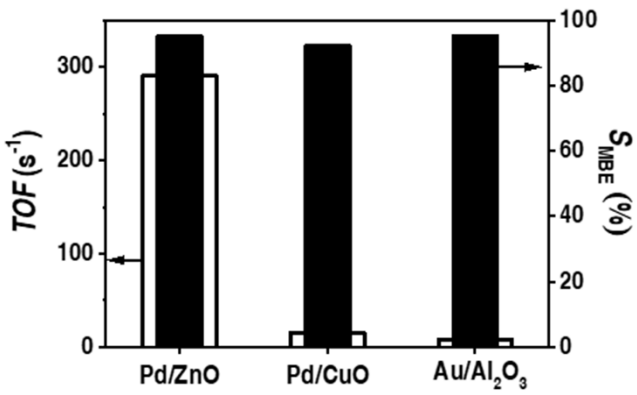

Figure 10: Variation of MBY transformation rate (*TOF,* s^{-1}; open bars) and MBE selectivity (S_{MBE}, %; solid bars) for reaction over Pd/ZnO, Pd/CuO and Au/Al_2O_3 activated at 573 K. *Reaction conditions*: $T = 403$ K, $P = 1$ atm, $X_{MBY} \sim 10\%$.

Au/Al_2O_3 and Pd/CuO with lower hydrogen uptake capacity (32-75 μmol g_{metal}^{-1} *vs.* 167 μmol g_{metal}^{-1}) delivered the lowest activity. Marin-Astorga *et al.*[85] reported a similar dependence of activity with H_2 uptake in the hydrogenation of C3-C5 alkynes over Pd/SiO_2 and Pd/MCM-41. Under the same conversion degree (X_{MBY} =10%), the three catalysts delivered a similar high selectivity (*ca.* 96%) to the target MBE ($S_{MBA} \sim 4\%$). Lin *et al.*[86] reported high S_{MBE} in liquid

phase operation over Au supported on active carbon, but we provide in here the first evidence of elevated MBE production in continuous gas phase operation.

The relationship between MBY conversion (X_{MBY}) and MBE selectivity (S_{MBE}) for Pd/ZnO, Pd/Al_2O_3 and industrial Lindlar catalyst shown in **Figure 11** provides an overall picture of the selectivity trends; the lines are intended merely as a guide to aid visual assessment and do not possess any "fitting" significance.

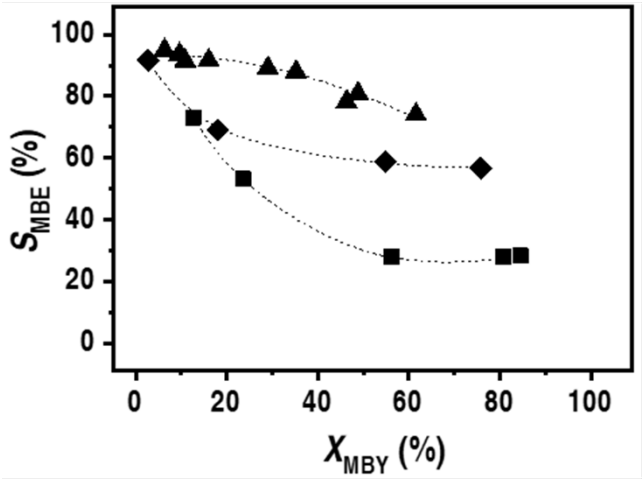

Figure 11: Variation of MBE selectivity (S_{MBE}, %) as a function of MBY conversion (X_{MBY}, %) for reaction over Pd/ZnO (▲), Pd/Al_2O_3 (■) and Lindlar's (◆) catalysts. *Note*: dashed lines provide a guide to aid visual assessment. *Reaction conditions*: T = 403 K, P = 1 atm.

In each case, S_{MBE} decreased (to varying degrees) as MBY conversion was increased. This anti-sympathetic correlation between X_{MBY} and S_{MBE} is to be expected in a stepwise hydrogenation scheme where total hydrogenation should be enhanced at greater X_{MBY}. We could not find any report of MBY hydrogenation promoted by supported Pd catalysts that has considered the dependence of S_{MBE} with X_{MBY}. It is, nonetheless, worth flagging the work of Kim and Moon[87] who observed a similar trend in the gas phase hydrogenation of acetylene over Pd/SiO_2. MBE selectivity over Pd/Al_2O_3 was significantly lower than that recorded for Pd/ZnO, regardless of MBY conversion. We observed an intermediate level of S_{MBE} over the Lindlar

catalyst at all MBY conversions, which can be tentatively ascribed to a decrease of $Pd^{\delta-}$ ensemble size by the Pd_3Pb alloy phase.[88] The higher MBE selectivity over Pd/ZnO (*vs.* Lindlar) can be explained by the increased temperature requirement for the generation of Pd_3Pb relative to β-PdZn[89] which, in turn, will result in a greater surface β-PdZn content at each temperature.

4. Conclusions

A series of Pd/ZnO catalysts with different β-PdZn alloy content were synthesized *via* deposition of *ex situ* generated Pd colloids followed by thermal treatment in H_2 to 403-973 K and used in the continuous gas phase hydrogenation of MBY→MBE. Powder XRD analysis confirmed alloy formation while XPS measurements revealed the coexistence of $Pd^{\delta-}$ and β-PdZn alloy on the catalyst surface with increase PdZn/$Pd^{\delta-}$ mol ratio at higher activation temperatures. Pd/ZnO was the most selective to the target MBE while (a benchmark) Pd/Al_2O_3 delivered the highest activity, regardless of reduction temperature in H_2. Both systems showed a similar dependence with activation temperature consistent with greater MBE selectivity and lower activity over catalysts prepared at higher temperature. We attributed this response to dilution of exposed $Pd^{\delta-}$ ensembles due to alloy formation and metal encapsulation (for Pd/ZnO) or metal agglomeration (in Pd/Al_2O_3). Pd/ZnO also delivered the best combined activity/MBE selectivity relative to industrial Lindlar catalyst, Pd/CuO and Au/Al_2O_3. Our results establish a direct correlation between surface β-PdZn alloy content and catalytic performance for the continuous gas phase transformation of alkenols with multiple industrial applications.

Acknowledgments

The authors acknowledge financial support from the Engineering and Physical Sciences Research Council EPSRC grant number EP/L016419/1 [Ph.D. studentship to Alberto González-

Fernández and Chiara Pischetola, CRITICAT program] and the Russian Science Foundation (project number 15-19-20023).

References

(1) Bieszczad, B.; Gilheany, D. G. Highly Stereoselective Construction of the C2 Stereocentre of α-Tocopherol (Vitamin E) by Asymmetric Addition of Grignard Reagents to Ketones. *Org. Biomol. Chem.* **2017**, *15* (31), 6483–6492.

(2) Lokko, Y.; Heijde, M.; Schebesta, K.; Scholtès, P.; Van Montagu, M.; Giacca, M. Biotechnology and the Bioeconomy—Towards Inclusive and Sustainable Industrial Development. *N. Biotechnol.* **2018**, *40*, 5–10.

(3) Crespo-Quesada, M.; Cárdenas-Lizana, F.; Dessimoz, A. L.; Kiwi-Minsker, L. Modern Trends in Catalyst and Process Design for Alkyne Hydrogenations. *ACS Catal.* **2012**, *2*, 1773–1786.

(4) Lee, S. L.; O'Connor, T. F.; Yang, X.; Cruz, C. N.; Chatterjee, S.; Madurawe, R. D.; Moore, C. M. V.; Yu, L. X.; Woodcock, J. Modernizing Pharmaceutical Manufacturing: From Batch to Continuous Production. *J. Pharm. Innov.* **2015**, *10* (3), 191–199.

(5) Moreno-Marrodan, C.; Liguori, F.; Barbaro, P. Continuous-Flow Processes for the Catalytic Partial Hydrogenation Reaction of Alkynes. *J. Org. Chem.* **2017**, *13*, 734–754.

(6) Crespo-Quesada, M.; Yarulin, A.; Jin, M.; Xia, Y.; Kiwi-Minsker, L. Structure Sensitivity of Alkynol Hydrogenation on Shape and Size Controlled Palladium Nanocrystals: Which Sites Are Most Active and Selective? *J. Am. Chem. Soc.* **2011**, *133* (32), 12787–12794.

(7) Studt, F.; Abild-Pedersen, F.; Bligaard, T.; Sørensen, R. Z.; Christensen, C. H.; Nørskov, J. K. On the Role of Surface Modifications of Palladium Catalysts in the Selective

Hydrogenation of Acetylene. *Angew. Chemie Int. Ed.* **2008**, *47* (48), 9299–9302.

(8) Dobrovolná, Z.; Kačer, P.; Červený, L. Competitive Hydrogenation in Alkene–Alkyne–Diene Systems with Palladium and Platinum Catalysts. *J. Mol. Catal. A Chem.* **1998**, *130* (3), 279–284.

(9) Sulman, E. M.; Matveeva, V.; Doluda, V.; Nikoshvili, L.; Bykov, A.; Demidenko, G.; Bronstein, L. Scientific Bases for the Preparation of Heterogeneous Catalysts. In *Preparation of the Polymer Stabilized and the Supported Nanostructured Catalysts*; Gaigneaux, E. M., Devillers, M., Hermans, S., Jacobs, P. A., Eds.; Elsevier: Leuven, 2010; pp 156–157.

(10) Molnár, Á.; Sárkány, A.; Varga, M. Hydrogenation of Carbon-Carbon Multiple Bonds: Chemo-, Regio- and Stereo-Selectivity. *J. Mol. Catal. A Chem.* **2001**, *173* (1–2), 185–221.

(11) Mei, D.; Neurock, M.; Smith, C. M. Hydrogenation of Acetylene–Ethylene Mixtures over Pd and Pd–Ag Alloys: First-Principles-Based Kinetic Monte Carlo Simulations. *J. Catal.* **2009**, *268* (2), 181–195.

(12) Berguerand, C.; Yuranov, I.; Cárdenas-Lizana, F.; Yuranova, T.; Kiwi-Minsker, L. Size-Controlled Pd Nanoparticles in 2-Butyne-1,4-Diol Hydrogenation: Support Effect and Kinetics Study. *J. Phys. Chem. C* **2014**, *118* (23), 12250–12259.

(13) Nijhuis, T. A.; Van Koten, G.; Moulijn, J. A. Optimized Palladium Catalyst Systems for the Selective Liquid-Phase Hydrogenation of Functionalyzed Alkynes. *Appl. Catal. A Gen.* **2003**, *238* (2), 259–271.

(14) López, N.; Vargas-Fuentes, C. Promoters in the Hydrogenation of Alkynes in Mixtures: Insights from Density Functional Theory. *Chem. Commun.* **2012**, *48* (10), 1379–1391.

(15) Coq, B.; Figueras, F. Bimetallic Palladium Catalysts: Influence of the Co-Metal on the

Catalyst Performance. *J. Mol. Catal. A Chem.* **2001**, *173* (1), 117–134.

(16) Bahruji, H.; Bowker, M.; Hutchings, G.; Dimitratos, N.; Wells, P.; Gibson, E.; Jones, W.; Brookes, C.; Morgan, D.; Lalev, G. Pd/ZnO Catalysts for Direct CO_2 Hydrogenation to Methanol. *J. Catal.* **2016**, *343*, 133–146.

(17) Tew, M. W.; Emerich, H.; Bokhoven, J. A. van. Formation and Characterization of PdZn Alloy: A Very Selective Catalyst for Alkyne Semihydrogenation. *J. Phys. Chem. C* **2011**, *115*, 8457–8465.

(18) Zhou, H.; Yang, X.; Li, L.; Liu, X.; Huang, Y.; Pan, X.; Wang, A.; Li, J.; Zhang, T. PdZn Intermetallic Nanostructure with Pd–Zn–Pd Ensembles for Highly Active and Chemoselective Semi-Hydrogenation of Acetylene. *ACS Catal.* **2016**, *6* (2), 1054–1061.

(19) Föttinger, K. PdZn Based Catalysts: Connecting Electronic and Geometric Structure with Catalytic Performance. In *Catalysis: Volume 25*; Spivey, J. J., Dooley, K. M., Ha, Y.-F., Eds.; Royal Society of Chemistry: Cambridge, 2013; pp 77–117.

(20) Karim, A. M.; Conant, T.; Datye, A. K. Controlling ZnO Morphology for Improved Methanol Steam Reforming Reactivity. *Phys. Chem. Chem. Phys.* **2008**, *10* (36), 5584–5590.

(21) Karim, A.; Conant, T.; Datye, A. The Role of PdZn Alloy Formation and Particle Size on the Selectivity for Steam Reforming of Methanol. *J. Catal.* **2006**, *243* (2), 420–427.

(22) Conant, T.; Karim, A. M.; Lebarbier, V.; Wang, Y.; Girgsdies, F.; Schlögl, R.; Datye, A. Stability of Bimetallic Pd–Zn Catalysts for the Steam Reforming of Methanol. *J. Catal.* **2008**, *257* (1), 64–70.

(23) Suwa, Y.; Ito, S.; Kameoka, S.; Tomishige, K.; Kunimori, K. Comparative Study between Zn–Pd/C and Pd/ZnO Catalysts for Steam Reforming of Methanol. *Appl. Catal. A Gen.*

2004, *267* (1–2), 9–16.

(24) Wei, Z.; Sun, J.; Li, Y.; Datye, A. K.; Wang, Y. Bimetallic Catalysts for Hydrogen Generation. *Chem. Soc. Rev.* **2012**, *41* (24), 7994–8008.

(25) Okhlopkova, L. B.; Matus, E. V.; Prosvirin, I. P.; Kerzhentsev, M. A.; Ismagilov, Z. R. Selective Hydrogenation of 2-Methyl-3-Butyn-2-ol Catalyzed by Embedded Polymer-Protected PdZn Nanoparticles. *J. Nanopart. Res.* **2015**, *17* (12), 475–490.

(26) Iwasa, N.; Takezawa, N. New Supported Pd and Pt Alloy Catalysts for Steam Reforming and Dehydrogenation of Methanol. *Top. Catal.* **2003**, *22* (3–4), 215–224.

(27) Segura, Y.; López, N.; Pérez-Ramírez, J. Origin of the Superior Hydrogenation Selectivity of Gold Nanoparticles in Alkyne + Alkene Mixtures: Triple- versus Double-Bond Activation. *J. Catal.* **2007**, *247* (2), 383–386.

(28) Maksimov, G. M.; Zaikovskii, V. I.; Matveev, K. I.; Likholobov, V. A. Preparation of Polyoxometalate-Stabilized Colloidal Solutions of Palladium Metal and Catalysts Supported on Them. *Kinet. Catal.* **2000**, *41* (6), 844–852.

(29) Maksimova, G. M.; Chuvilin, A. L.; Moroz, E. M.; Likholobov, V. A.; Matveev, K. I. Preparation of Colloidal Solutions of Noble Metals Stabilized by Polyoxometalates and Supported Catalysts Based on These Solutions. *Kinet. Catal.* **2004**, *45* (6), 870–878.

(30) Khoudiakov, M.; Gupta, M. C.; Deevi, S. Au/Fe_2O_3 Nanocatalysts for CO Oxidation: A Comparative Study of Deposition–Precipitation and Coprecipitation Techniques. *Appl. Catal. A Gen.* **2005**, *291* (1–2), 151–161.

(31) Lindlar, H.; Dubuis, R. Palladium Catalyst for Partial Reduction of Acetylenes. In *Organic Syntheses*; John Wiley & Sons, Inc.: Hoboken, NJ, USA, 2003; Vol. 46, pp 89–89.

(32) Venezia, A. M.; Duca, D.; Floriano, M. A.; Deganello, G.; Rossi, A. XPS Study of

Pumice-Supported Palladium and Platinum Catalysts. *Surf. Interface Anal.* **1992**, *19* (1–12), 543–547.

(33) Turner, N. H.; Single, A. M. Determination of Peak Positions and Areas from Wide-Scan XPS Spectra. *Surf. Interface Anal.* **1990**, *15* (3), 215–222.

(34) Zhong, J. B.; Li, J. Z.; He, X. Y.; Zeng, J.; Lu, Y.; Hu, W.; Lin, K. Improved Photocatalytic Performance of Pd-Doped ZnO. *Curr. Appl. Phys.* **2012**, *12* (3), 998–1001.

(35) Jana, R.; Subbarao, U.; Peter, S. C. Ultrafast Synthesis of Flower-like Ordered Pd_3Pb Nanocrystals with Superior Electrocatalytic Activities towards Oxidation of Formic Acid and Ethanol. *J. Power Sources* **2016**, *301*, 160–169.

(36) Hachemi, I.; Jeništová, K.; Mäki-Arvela, P.; Kumar, N.; Eränen, K.; Hemming, J.; Murzin, D. Y. Comparative Study of Sulfur-Free Nickel and Palladium Catalysts in Hydrodeoxygenation of Different Fatty Acid Feedstocks for Production of Biofuels. *Catal. Sci. Technol.* **2016**, *6* (5), 1476–1487.

(37) N. Iwasa, S. Masuda, N. Ogawa, N. T. Steam Reforming of Methanol over Pd/ZnO: Effect of the Formation of PdZn Alloys upon the Reaction. *Appl. Catal. A Gen.* **1995**, *125* (1), 145–157.

(38) Wang, C.-B.; Gau, G.-Y.; Gau, S.-J.; Tang, C.-W.; Bi, J.-L. Preparation and Characterization of Nanosized Nickel Oxide. *Catal. Lett.* **2005**, *101* (3–4), 241–247.

(39) Gómez-Quero, S.; Cárdenas-Lizana, F.; Keane, M. A. Effect of Metal Dispersion on the Liquid-Phase Hydrodechlorination of 2,4-Dichlorophenol over Pd/Al_2O_3. *Ind. Eng. Chem. Res.* **2008**, *47* (18), 6841–6853.

(40) Iwasa, N.; Ogawa, N.; Masuda, S.; Takezawa, N. Selective PdZn Alloy Formation in the Reduction of Pd/ZnO Catalysts. *Bull. Chem. Soc. Jpn.* **1998**, *71* (6), 1451–1455.

(41) Penner, S.; Jenewein, B.; Gabasch, H.; Klötzer, B.; Wang, D.; Knop-Gericke, A.; Schlögl, R.; Hayek, K. Growth and Structural Stability of Well-Ordered PdZn Alloy Nanoparticles. *J. Catal.* **2006**, *241* (1), 14–19.

(42) Kniep, B. L.; Girgsdies, F.; Ressler, T. Effect of Precipitate Aging on the Microstructural Characteristics of Cu/ZnO Catalysts for Methanol Steam Reforming. *J. Catal.* **2005**, *236* (1), 34–44.

(43) Liu, J.; Qiao, B.; Song, Y.; Tang, H.; Huang, Y.; Liu, J. Highly Active and Sintering-Resistant Heteroepitaxy of Au Nanoparticles on ZnO Nanowires for CO Oxidation. *J. Energy Chem.* **2016**, *25* (3), 361–370.

(44) Tran, S. B. T.; Choi, H. S.; Oh, S. Y.; Moon, S. Y.; Park, J. Y. Iron-Doped ZnO as a Support for Pt-Based Catalysts to Improve Activity and Stability: Enhancement of Metal–Support Interaction by the Doping Effect. *RSC Adv.* **2018**, *8* (38), 21528–21533.

(45) Lv, Y.; Yao, W.; Ma, X.; Pan, C.; Zong, R.; Zhu, Y. The Surface Oxygen Vacancy Induced Visible Activity and Enhanced UV Activity of a ZnO_{1-x} Photocatalyst. *Catal. Sci. Technol.* **2013**, *3* (12), 3136–3146.

(46) Wang, Y.; Zhang, J.; Xu, H. Interaction between Pd and ZnO during Reduction of Pd/ZnO Catalyst for Steam Reforming of Methanol to Hydrogen. *Chin. J. Catal.* **2006**, *27* (3), 217–222.

(47) Castillejos-López, E.; Agostini, G.; Di Michel, M.; Iglesias-Juez, A.; Bachiller-Baeza, B. Synergy of Contact between ZnO Surface Planes and PdZn Nanostructures: Morphology and Chemical Property Effects in the Intermetallic Sites for Selective 1,3-Butadiene Hydrogenation. *ACS Catal.* **2017**, *7* (1), 796–811.

(48) Campbell, C. T.; Sellers, J. R. V. Anchored Metal Nanoparticles: Effects of Support and

Size on Their Energy, Sintering Resistance and Reactivity. *Faraday Discuss.* **2013**, *162* (9), 9–30.

(49) Liewhiran, C.; Phanichphant, S. Doctor-Bladed Thick Films of Flame-Made Pd/ZnO Nanoparticles for Ethanol Sensing. *Curr. Appl. Phys.* **2008**, *8* (3–4), 336–339.

(50) Lee, I.; Morales, R.; Albiter, M. A.; Zaera, F. Synthesis of Heterogeneous Catalysts with Well Shaped Platinum Particles to Control Reaction Selectivity. *PNAS* **2008**, *105* (40), 15241–15246.

(51) Tonetto, G. M.; Damiani, D. E. Performance of Pd-Mo/γ-Al_2O3 Catalysts for the Selective Reduction of NO by Methane. *J. Mol. Catal. A Chem.* **2003**, *202* (1–2), 289–303.

(52) Parks, G. A. The Isoelectric Points of Solid Oxides, Solid Hydroxides, and Aqueous Hydroxo Complex Systems. *Chem. Rev.* **1965**, *65* (2), 177–198.

(53) Webber, P. R.; Rojas, C. E.; Dobson, P. J.; Chadwick, D. A Combined XPS/AES Study of Cu Segregation to the High and Low Index Surfaces of a Cu-Ni Alloy. *Surf. Sci.* **1981**, *105* (1), 20–40.

(54) Moulder, J. F.; Chastain, J.; King, R. C. Standard XPS Spectra of Elements. In *Handbook of X-ray Photoelectron Spectroscopy*; Chastain, J., Ed.; Perkin-Elmer Corporation: Minnesota, 1992; pp 118–119.

(55) Liqiang, J.; Wang, B.; Baifu, X.; Shudan, L.; Keying, S.; Weimin, C.; Honggang, F. Investigations on the Surface Modification of ZnO Nanoparticle Photocatalyst by Depositing Pd. *J. Solid State Chem.* **2004**, *177* (11), 4221–4227.

(56) Wang, H.; Gu, X.-K.; Zheng, X.; Pan, H.; Zhu, J.; Chen, S.; Cao, L.; Li, W.-X.; Lu, J. Disentangling the Size-Dependent Geometric and Electronic Effects of Palladium Nanocatalysts beyond Selectivity. *Sci. Adv.* **2019**, *5* (1), 1-8.

(57) Gigola, C. E.; Moreno, M. S.; Costilla, I.; Sánchez, M. D. Characterization of Pd–CeO_x Interaction on α-Al_2O_3 Support. *Appl. Surf. Sci.* **2007**, *254* (1), 325–329.

(58) Sárkány, A.; Zsoldos, Z.; Furlong, B.; Hightower, J. W.; Guczi, L. Hydrogenation of 1-Butene and 1,3-Butadiene Mixtures over Pd/ZnO Catalysts. *J. Catal.* **1993**, *141* (2), 566–582.

(59) Monteiro, R. S.; Dieguez, L. C.; Schmal, M. The Role of Pd Precursors in the Oxidation of Carbon Monoxide over Pd/Al_2O_3 and Pd/CeO_2/Al_2O_3 Catalysts. *Catal. Today* **2001**, *65* (1), 77–89.

(60) Lederhos, C.; Betti, C.; Liprandi, D.; Cagnola, E.; Quiroga, M. Alkyne Selective Hydrogenation with Mono- and Bimetallic-Anchored Catalysts. In *New Advances in Hydrogenation Processes - Fundamentals and Applications*; Ravanchi, M. T., Ed.; InTech: Rijeka, 2017; pp 15–36.

(61) Horiuti, I.; Polanyi, M. Exchange Reactions of Hydrogen on Metallic Catalyst. *Trans. Faraday Soc.* **1934**, *30*, 1164–1172.

(62) Karavanov, A. N.; Gryaznov, V. M. Effect of the Structure of Substituted Propargyl and Allyl Alcohols on the Rate of Their Liquid Phase Hydrogenation on a Pd-Ru Alloy Membrane Catalyst. *Bull. Acad. Sci. USSR, Div. Chem. Sci.* **1989**, *38* (8), 1593–1596.

(63) Sheth, P. A.; Neurock, M.; Smith, C. M. A First-Principles Analysis of Acetylene Hydrogenation over Pd(111). *J. Phys. Chem. B* **2003**, *107* (9), 2009–2017.

(64) Mei, D.; Sheth, P.; Neurock, M.; Smith, C. First-Principles-Based Kinetic Monte Carlo Simulation of the Selective Hydrogenation of Acetylene over Pd(111). *J. Catal.* **2006**, *242* (1), 1–15.

(65) Sárkány, A.; Horváth, A.; Beck, A. Hydrogenation of Acetylene over Low Loaded Pd and

Pd-Au/SiO_2 Catalysts. *Appl. Catal. A Gen.* **2002**, *229* (1), 117–125.

(66) Kranich, W. L.; Weiss, A. H.; Schay, Z.; Guczi, L. Acetylene Hydrogenation Using Palladium Zeolite Catalysts. *Appl. Catal.* **1985**, *13* (2), 257–267.

(67) McCue, A. J.; Guerrero-Ruiz, A.; Rodríguez-Ramos, I.; Anderson, J. A. Palladium Sulphide – A Highly Selective Catalyst for the Gas Phase Hydrogenation of Alkynes to Alkenes. *J. Catal.* **2016**, *340*, 10–16.

(68) Nikolaev, S. A.; Zanaveskin, L. N.; Smirnov, V. V.; Averyanov, V. A.; Zanaveskin, K. L. Catalytic Hydrogenation of Alkyne and Alkadiene Impurities from Alkenes. Practical and Theoretical Aspects. *Russ. Chem. Rev.* **2009**, *78* (3), 231–247.

(69) Newton, M. D.; Lipscomb, W. N. Interaction of a Methyl Group with a Triple Bond. Molecular Self-Consistent Field Calculation on Methylacetylene. *J. Am. Chem. Soc.* **1967**, *89* (17), 4261–4267.

(70) Allenger, V. M.; McLean, D. D.; Ternan, M. Simultaneous Polymerization and Oligomerization of Acetylene on Alumina and Fluoridated Alumina Catalysts. *J. Catal.* **1991**, *131* (2), 305–318.

(71) Protasova, L. N.; Rebrov, E. V.; Choy, K. L.; Pung, S. Y.; Engels, V.; Cabaj, M.; Wheatley, A. E. H.; Schouten, J. C. ZnO Based Nanowires Grown by Chemical Vapour Deposition for Selective Hydrogenation of Acetylene Alcohols. *Catal. Sci. Technol.* **2011**, *1* (5), 768–777.

(72) Mohr, C.; Claus, P. Hydrogenation Properties of Supported Nanosized Gold Particles. *Sci. Prog.* **2001**, *84* (4), 311–334.

(73) Xie, S.; Choi, S. I.; Xia, X.; Xia, Y. Catalysis on Faceted Noble-Metal Nanocrystals: Both Shape and Size Matter. *Curr. Opin. Chem. Eng.* **2013**, *2* (2), 142–150.

(74) Chen, Y.-J.; Yeh, C. Deposition of Highly Dispersed Gold on Alumina Support. *J. Catal.* **2001**, *200* (1), 59–68.

(75) Hao, Z.; An, L.; Wang, H. Catalytic Performance and Structural Characterization of Ferric Oxide and Its Composite Oxides Supported Gold Catalysts for Low-Temperature CO Oxidation. *Sci. China Ser. B Chem.* **2001**, *44* (6), 596–605.

(76) Jiang, T.; Huai, Q.; Geng, T.; Ying, W.; Xiao, T.; Cao, F. Catalytic Performance of Pd–Ni Bimetallic Catalyst for Glycerol Hydrogenolysis. *Biomass Bioenerg.* **2015**, *78*, 71–79.

(77) Ding, E.; Jujjuri, S.; Sturgeon, M.; Shore, S. G.; Keane, M. A. Novel One Step Preparation of Silica Supported Pd/Sr and Pd/Ba Catalysts *via* an Organometallic Precursor: Application in Hydrodechlorination and Hydrogenation. *J. Mol. Catal. A Chem.* **2008**, *294* (1–2), 51–60.

(78) Pei, G. X.; Liu, X. Y.; Yang, X.; Zhang, L.; Wang, A.; Li, L.; Wang, H.; Wang, X.; Zhang, T. Performance of Cu-Alloyed Pd Single-Atom Catalyst for Semihydrogenation of Acetylene under Simulated Front-End Conditions. *ACS Catal.* **2017**, *7* (2), 1491–1500.

(79) Yin, M.; Wu, C.-K.; Lou, Y.; Burda, C.; Koberstein, J. T.; Zhu, Y.; O'brien, S. Copper Oxide Nanocrystals. *J. Am. Chem. Soc.* **2005**, *127* (26), 9506–9511.

(80) Srikant, V.; Clarke, D. R. On the Optical Band Gap of Zinc Oxide. *J. Appl. Phys.* **1998**, *83* (10), 5447–5451.

(81) Bond, G. C.; Louis, C.; Thompson, D. T. Chemisorbtion of Simple Molecules on Gold. In *Catalysis by Gold*; Imperial College Press, Ed.; World Scientific: London, 2006; Vol. 6, pp 121–160.

(82) Meshesha, B. T.; Barrabés, N.; Llorca, J.; Dafinov, A.; Medina, F.; Föttinger, K. PdCu Alloy Nanoparticles on Alumina as Selective Catalysts for Trichloroethylene

Hydrodechlorination to Ethylene. *Appl. Catal. A Gen.* **2013**, *453*, 130–141.

(83) Lopez, N.; Nørskov, J. K.; Janssens, T. V. W.; Carlsson, A.; Puig-Molina, A.; Clausen, B. S.; Grunwaldt, J.-D. The Adhesion and Shape of Nanosized Au Particles in a Au/TiO_2 Catalyst. *J. Catal.* **2004**, *225* (1), 86–94.

(84) Haruta, M.; Daté, M. Advances in the Catalysis of Au Nanoparticles. *Appl. Catal. A Gen.* **2001**, *222* (1–2), 427–437.

(85) Marın-Astorga, N.; Pecchi, G.; Fierro, J. L. G.; Reyes, P. Alkynes Hydrogenation over Pd-Supported Catalysts. *Catal. Lett.* **2003**, *91* (1), 115–121.

(86) Lin, R.; Albani, D.; Fako, E.; Kaiser, S. K.; Safonova, O. V.; López, N.; Pérez-Ramírez, J. Design of Single Gold Atoms on Nitrogen-Doped Carbon for Molecular Recognition in Alkyne Semi-Hydrogenation. *Angew. Chemie* **2019**, *131* (2), 514–519.

(87) Kim, W.-J.; Moon, S. H. Modified Pd Catalysts for the Selective Hydrogenation of Acetylene. *Catal. Today* **2012**, *185* (1), 2–16.

(88) Anderson, J.; Mellor, J.; Wells, R. Pd Catalysed Hexyne Hydrogenation Modified by Bi and by Pb. *J. Catal.* **2009**, *261* (2), 208–216.

(89) Furukawa, S.; Komatsu, T. Selective Hydrogenation of Functionalized Alkynes to (E)-Alkenes, Using Ordered Alloys as Catalysts. *ACS Catal.* **2016**, *6* (3), 2121–2125.

Table of Contents Image